Valley filtering in 8-*Pmmn* borophene based on an electrostatic waveguide constriction

Emile Vanderstraeten* and Dries Vande Ginste

quest, IDLab, Department of Information Technology, Ghent University/imec, Technologiepark-Zwijnaarde 126, 9000 Ghent, Belgium

(Received 10 August 2023; revised 24 April 2024; accepted 26 April 2024; published 9 May 2024)

Materials with tilted Dirac cones, such as 8-*Pmmn* borophene, are being explored for valleytronic applications as the tilting direction is different for nonequivalent valleys. In this paper, a valley-filtering device based on electrostatic waveguides is proposed. First, these waveguides are examined from a theoretical point of view. An inner product is defined starting from the probability current density along the waveguide axis. It is shown that the bound modes with real eigenvalues are mutually orthogonal and orthogonal with respect to all radiating modes. In a next step, by exploiting these orthogonality properties, a simulation procedure is introduced based on an explicit, symplectic partitioned Runge-Kutta time-stepping method specifically adapted for this problem. Finally, this approach is applied to the situation of a waveguide nanoconstriction and it is demonstrated that this structure can function as a valley filter. Within a certain window in the energy domain, transmission is practically zero for one valley, while being almost perfect for the other one. The effect of several design variables, such as length and width of the constriction, is carefully investigated. Moreover, the effect of misalignment between the tilting direction and the waveguide axis is assessed, showing that the proposed valley-filtering design is robust against deviations up to several tens of degrees. In addition, the simulation results reveal that the dispersion relation of the waveguide modes is not necessarily monotonic, which can give rise to oscillations in the transmission function due to interference effects.

DOI: 10.1103/PhysRevB.109.205413

I. INTRODUCTION

Low-energy excitations in materials such as graphene, topological insulators, and Dirac semimetals behave as massless Dirac particles [1]. The charge carriers in these materials, also called Dirac materials, adhere to a linear instead of a parabolic dispersion relation. Hence, they exhibit remarkable similarities with light and for several optical phenomena an analog can be found in the aforementioned materials. The refraction and reflection of a Dirac particle incident on a *pn* junction is comparable to light incident on a layer with a different refractive index and the angle of refraction obeys Snell's law in which the refractive index has been replaced by the kinetic energy [2]. Several potential applications have been proposed that exploit this peculiar scattering behavior, such as Veselago lenses [3], transistors [4–7], and reflectors [8], while the theoretical foundations have been experimentally verified in graphene in [9,10]. The domain of electron optics is not restricted to only scattering at *pn* junctions; electronic analogs of the Goos-Hänchen effect [11,12], zero-index metamaterials [13], gradient-index optics [14], and waveguides have been investigated as well. Even though it is difficult to confine particles in Dirac materials because of the Klein tunneling effect, it has been demonstrated that one-dimensional waveguides can be created in graphene by employing electrostatically induced quantum wells [15–22], barriers [23], and combinations thereof [21]. In contrast to nanoribbons, another possible realization of a one-dimensional electronic channel in graphene, these waveguides are well separated from the edges and thus they do not suffer from edge scattering [16]. The existence of the guided modes has been experimentally verified for a quantum well that was electrostatically induced by a charged carbon nanotube in [20].

Recently, materials with tilted anisotropic Dirac cones have attracted considerable interest. Compared to the Dirac cones of graphene and other, ordinary Dirac materials, these tilted Dirac cones are not rotationally invariant and the axes of the cones exhibit a tilt with respect to the energy axis [24]. Tilted Dirac cones are expected for the quasi-two-dimensional organic conductor α-(BEDT-TTF)$_2$I$_3$ [25–27], quinoid graphene [26], hydrogenated graphene [28], 8-*Pmmn* borophene [29–32], and $1T'$-MoS_2 [33]. 8-*Pmmn* borophene is a two-dimensional allotrope of boron and consists of two nonequivalent buckled sublattices [24]. By means of a first-principles numerical method it has been predicted that its dispersion relation contains two nonequivalent Dirac cones, $\boldsymbol{k}_D$ and $-\boldsymbol{k}_D$, that have an opposite tilting direction [29,30]. Similarly as for graphene, a continuum Hamiltonian has been derived for the low-energy excitations starting from a tight-binding description [31]. The tilted Dirac dispersion holds for energies up to approximately 1 eV [24], which makes this material an ideal test bed to explore the physics associated with tilted Dirac cones. Moreover, in recent years much progress has been made in the synthesis of different types of two-dimensional boron allotropes by means of molecular beam epitaxy, liquid-phase exfoliation, and micromechanical exfoliation [34–38], paving the way for future use in nanoelectronic devices.

*Emile.Vanderstraeten@UGent.be

Several papers have addressed the *pn* junction and the *npn* junction in 8-*Pmmn* borophene [39–45]. It has been demonstrated that perfect transmission through a potential barrier now occurs at a nonzero incidence angle, i.e., oblique Klein tunneling [39,40,42]. Additionally, the locking relation between momentum and velocity has been lifted, enabling electron retroreflection at a *pn* junction [40]. Moreover, as the valleys, $\boldsymbol{k}_D$ and $-\boldsymbol{k}_D$, exhibit a different tilting direction, 8-*Pmmn* borophene is also an alluring material for valleytronic applications. Valley-filtering devices have been proposed based on the Goos-Hänchen effect [45], on magnetic-electric barriers [46], and on superlattice structures [47]. In [45,47] the valley filtering is achieved by an electrostatic potential that is discontinuous; such a potential is hard to realize experimentally in two-dimensional materials [48]. In [46], an additional vector potential is required to achieve valley filtering. In [49], it has been shown that the eigenmodes of a straight electrostatically induced waveguide in the presence of tilting can be related to the eigenmodes of the untilted situation by means of a simple transformation. After a subsequent theoretical study of the eigenmodes of a waveguide defined by a smooth hyperbolic secant potential, for which analytical solutions can be found, it was suggested that these electrostatically induced waveguides could be of use in valleytronic applications. In this paper, however, we take it a step further and propose a concrete valley-filtering device based on a nanoconstriction in a waveguide in 8-*Pmmn* borophene obtained by means of a smooth electrostatic potential. Our proposal is threefold. First, we demonstrate that the two valleys exhibit different transmission properties through a waveguide constriction and we exploit this to propose a concrete topology of a valley filter in 8-*Pmmn* borophene. Second, we thoroughly study the properties of the entire device by means of numerical experiments, using a conservative, explicit partitioned Runge-Kutta time-stepping method [50], which is here specifically adapted to the tilted Dirac equation. This study yields insight into the working of such structure and clarifies the impact that various geometrical parameters have on the performance of the device. In addition, as it is from an experimental standpoint not possible to exactly set the orientation of the top gate with respect to the lattice of the Dirac material, the nonideal situation, for which the axis of the waveguide deviates from the tilting direction, is investigated as well. Third, an inner product is introduced based on the probability current density and the orthogonality relations are thoroughly examined. Note that these relations are derived for the specific waveguide problem at hand and do not straightforwardly follow from the traditional orthogonality analysis used in quantum mechanics (QM). Besides providing us valuable information concerning the properties of the different eigenmodes, these orthogonality relations are necessary for the efficient calculation of the transmission function in combination with the time-stepping method discussed in this paper. One single simulation run returns the transmission function for a wide range of energies.

The outline of this paper is as follows. First, the waveguide's eigenmodes are discussed from a theoretical point of view in Sec. II. Special attention is given to the orthogonality of the eigenmodes. Afterward, in Sec. III, the numerical modeling method, which is based on a conservative time-stepping algorithm, is detailed. In Sec. IV it is demonstrated that a waveguide nanoconstriction constitutes an excellent valley filter and, in addition to the effect of several design parameters, misalignment between the tilting direction and the waveguide is investigated as well. Finally, the findings of this paper are summarized in Sec. V.

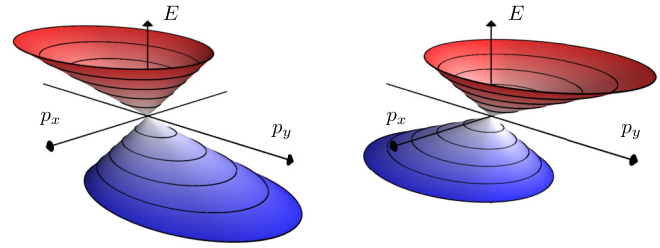

FIG. 1. Plot of the two nonequivalent Dirac cones of 8-*Pmmn* borophene for $V = 0$. The left (right) plot relates to the valley index τ equal to 1 (-1).

II. THEORY

A. Generalized eigenvalue problem

The tilted Dirac equation in 8-*Pmmn* borophene has the form [31]

$$i\hbar\frac{\partial}{\partial t}\Psi = [\tau(v_x\sigma_x p_x + v_y\sigma_y p_y + v_t\sigma_0 p_y) + V\sigma_0]\Psi, \quad (1)$$

with $\Psi = \binom{u}{v}$ the two-component wave function and $\sigma_x = \left(\begin{smallmatrix}0 & 1\\ 1 & 0\end{smallmatrix}\right)$, $\sigma_y = \left(\begin{smallmatrix}0 & -i\\ i & 0\end{smallmatrix}\right)$ the Pauli spin matrices. The matrix σ_0 is the unit matrix, while p_x and p_y are momentum operators. The potential energy is represented by V and depends on the position. The constants v_x, v_y, and v_t have as values 0.86×10^6 m/s, 0.69×10^6 m/s, and 0.32×10^6 m/s, respectively [31]. The variable τ, the valley index, is equal to 1 for $\boldsymbol{k}_D$ and -1 for $-\boldsymbol{k}_D$. The corresponding dispersion relation for $V = 0$ is given by

$$E = \tau v_t p_y \pm \sqrt{(v_x p_x)^2 + (v_y p_y)^2}, \quad (2)$$

which is plotted in Fig. 1. It is evident that the Dirac cone is not rotationally symmetric and that the axis of the cone exhibits a tilting with respect to the E axis. The equal-energy lines are ellipses for the tilted Dirac equation instead of circles as for the standard Dirac cone.

In the remainder of this section, it is assumed that V is y invariant and, thus, that the propagation direction of the waveguide is the y direction. Consequently, the following substitutions, $u(x, y, t) = u'(x)e^{i(k_y y-\omega t)}$ and $v(x, y, t) = v'(x)e^{i(k_y y-\omega t)}$, are introduced into (1), yielding

$$k_y\begin{pmatrix}\tau v_t & -i\tau v_y\\ i\tau v_y & \tau v_t\end{pmatrix}\begin{pmatrix}u'\\ v'\end{pmatrix} = \begin{pmatrix}\frac{E-V(x)}{\hbar} & i\tau v_x\frac{d}{dx}\\ i\tau v_x\frac{d}{dx} & \frac{E-V(x)}{\hbar}\end{pmatrix}\begin{pmatrix}u'\\ v'\end{pmatrix}, \quad (3)$$

a generalized eigenvalue problem, with k_y the eigenvalue and $\binom{u'}{v'}$ the eigenmode. Note that the energy E ($= \hbar\omega$) is a *parameter* here. Even though the other situation, with k_y as parameter and E as eigenvalue, is a well-studied problem in QM, we did not opt for it because of the following reasoning.

Consider a mode characterized by a certain E and k_y injected into the waveguide. Because the employed potentials are time independent, the energy E of the injected mode is conserved, in contrast to k_y, and hence, this means that in the waveguide structure only modes with the same energy E are excited. To determine these and their relevant expansion coefficients, it is more logical to investigate the generalized eigenvalue problem of (3) instead of its traditional QM counterpart.

It is easily verified that (3) can be rewritten as

$$k_y\begin{pmatrix}\tau v_t & \tau v_y\\ \tau v_y & \tau v_t\end{pmatrix}\begin{pmatrix}u'\\ -iv'\end{pmatrix}=\begin{pmatrix}\frac{E-V(x)}{\hbar} & -\tau v_x\frac{d}{dx}\\ \tau v_x\frac{d}{dx} & \frac{E-V(x)}{\hbar}\end{pmatrix}\begin{pmatrix}u'\\ -iv'\end{pmatrix}. \tag{4}$$

Equation (4) shows that one can choose u' real and v' purely imaginary if k_y is real. Additionally, it also follows that if k_y is an eigenvalue related to the eigenmode $\binom{u'}{v'}$, then the complex conjugate k_y^*, together with $\binom{u'^*}{-v'^*}$, satisfies (3) as well. Without tilting ($v_t = 0$), k_y being an eigenvalue related to the eigenmode $\binom{u'}{v'}$ implies that $-k_y$ is an eigenvalue related to the eigenmode $\binom{v'}{u'}$. It is evident that, because of the tilting, this property does not hold in general for the tilted Dirac equation.

B. Orthogonality relations

In a next step, we intend to define a suitable inner product as the orthogonality relations will be of use in Sec. III to construct an efficient numerical procedure. In the traditional QM analysis, where k_y is a parameter and E the eigenvalue, the orthogonality relations of the eigenmodes with respect to the inner product

$$\langle\Psi_1,\Psi_2\rangle=\int_{-\infty}^{+\infty}dx\,\Psi_2^\dagger\Psi_1 \tag{5}$$

immediately follow from the Hamiltonian being a self-adjoint operator. However, in this work, where E is a parameter and k_y the eigenvalue, the operator

$$\begin{pmatrix}\tau v_t & \tau v_y\\ \tau v_y & \tau v_t\end{pmatrix}^{-1}\begin{pmatrix}\frac{E-V(x)}{\hbar} & -\tau v_x\frac{d}{dx}\\ \tau v_x\frac{d}{dx} & \frac{E-V(x)}{\hbar}\end{pmatrix} \tag{6}$$

is not self-adjoint. Moreover, numerical tests have pointed out that two different eigenmodes Ψ_1 and Ψ_2, characterized by different eigenvalues $k_{y,1}$ and $k_{y,2}$ for the same energy E, are not orthogonal with respect to (5). Consequently, a different inner product needs to be considered to discuss the orthogonality properties of the eigenmodes.

Before proceeding to this inner product, an expression for the probability current density is first needed. Therefore, take the adjoint of (1) and right-multiply it by Ψ. Additionally, left-multiply (1) by $\Psi^\dagger$. Subtracting both results yields

$$\frac{\partial\Psi^\dagger\Psi}{\partial t}+\nabla_{xy}\cdot[\tau(v_t\boldsymbol{u}_y\Psi^\dagger\Psi+\Psi^\dagger\boldsymbol{\sigma}\Psi)]=0, \tag{7}$$

with $\nabla_{xy}=\frac{\partial}{\partial x}\boldsymbol{u}_x+\frac{\partial}{\partial y}\boldsymbol{u}_y$, where $\boldsymbol{u}_x$ and $\boldsymbol{u}_y$ are the unit vectors along the x and y axes, respectively, and $\boldsymbol{\sigma}=v_x\sigma_x\boldsymbol{u}_x+v_y\sigma_y\boldsymbol{u}_y$. Equation (7) corresponds to a continuity equation, and consequently, an expression for the particle probability current density is found, viz.,

$$\boldsymbol{j}=\tau(v_t\boldsymbol{u}_y\Psi^\dagger\Psi+\Psi^\dagger\boldsymbol{\sigma}\Psi). \tag{8}$$

Whereas the second term $\tau\Psi^\dagger\boldsymbol{\sigma}\Psi$ was expected, an additional term $\tau v_t\boldsymbol{u}_y\Psi^\dagger\Psi$ is now also present in the expression for the particle current density because of the tilting. This term is proportional to the position probability density $\Psi^\dagger\Psi$. Note further that $\boldsymbol{j}$ is real-valued.

Inspired by the expression for the probability current density, the following inner product is proposed:

$$\langle\Psi_1,\Psi_2\rangle=\int_{-\infty}^{+\infty}dx\begin{pmatrix}u_2'^* & v_2'^*\end{pmatrix}\begin{pmatrix}\tau v_t & -i\tau v_y\\ i\tau v_y & \tau v_t\end{pmatrix}\begin{pmatrix}u_1'\\ v_1'\end{pmatrix}. \tag{9}$$

If $\Psi_1=\Psi_2$, the integrand equals the y component of (8) and $\langle\Psi_1,\Psi_1\rangle$ is interpreted as the total particle current through the cross section of the waveguide for that particular mode with eigenvalue $k_{y,1}$. Note that in (9) it was implicitly assumed—for simplicity but without loss of generality—that $y=0$; otherwise an additional, exponential term is present in front of the integral depending on y and both eigenvalues, $k_{y,1}$ and $k_{y,2}$.

To discuss general properties regarding orthogonality, as a first step, (3) is substituted into (9), yielding

$$\frac{1}{k_{y,1}}\int_{-\infty}^{+\infty}dx\begin{pmatrix}u_2'^* & v_2'^*\end{pmatrix}\begin{pmatrix}\frac{E-V(x)}{\hbar} & i\tau v_x\frac{d}{dx}\\ i\tau v_x\frac{d}{dx} & \frac{E-V(x)}{\hbar}\end{pmatrix}\begin{pmatrix}u_1'\\ v_1'\end{pmatrix}. \tag{10}$$

Next, the eigenmodes of the waveguide are assumed to vanish at infinity. This way, the position of the eigenmodes can be interchanged by means of integration by parts:

$$\frac{1}{k_{y,1}}\left[\int_{-\infty}^{+\infty}dx\begin{pmatrix}u_1'^* & v_1'^*\end{pmatrix}\begin{pmatrix}\frac{E-V(x)}{\hbar} & i\tau v_x\frac{d}{dx}\\ i\tau v_x\frac{d}{dx} & \frac{E-V(x)}{\hbar}\end{pmatrix}\begin{pmatrix}u_2'\\ v_2'\end{pmatrix}\right]^*. \tag{11}$$

Finally, using (3) again, and since $\langle\Psi_1,\Psi_2\rangle^*=\langle\Psi_2,\Psi_1\rangle$, the following expression is obtained,

$$k_{y,1}\langle\Psi_1,\Psi_2\rangle=k_{y,2}^*\langle\Psi_1,\Psi_2\rangle. \tag{12}$$

Equation (12) gives us important insights into the properties of the eigenmodes. First, assume that the two modes are equal, so we are investigating the inner product of a mode with itself. In this case, if the inner product is nonzero, and thus the propagation of the mode along y corresponds to a nonzero particle flow, then the eigenmode is associated with a real eigenvalue. If the eigenvalue is complex, this necessarily leads to $\langle\Psi,\Psi\rangle$ being zero for the corresponding eigenmode Ψ. Note that the amplitude of a mode with real eigenvalue is constant along y; only the phase factor $e^{ik_y y}$ changes. For a mode with complex eigenvalue $k_y=\beta+\alpha i$, propagation along the y axis results in a factor $e^{i\beta y}e^{-\alpha y}$, affecting both phase and amplitude. Consequently, for $\alpha>0$, propagation along y entails an additional damping factor.

In a next step, the situation in which the two eigenmodes differ from each other is investigated. If the two eigenmodes correspond to two distinct real eigenvalues, then it is clear that the eigenmodes will be orthogonal according to the inner product defined by (9). Even when one of the eigenvalues is real and the other one complex, the eigenmodes are still orthogonal. Only when both eigenvalues are complex and when $k_{y,1}=k_{y,2}^*$, then the eigenmodes are not necessarily orthogonal. Thus, these eigenmodes do not diagonalize the probability

current density operator, which implies that a linear combination of these complex eigenmodes can still result in a nonzero particle flow along the y direction even though $\langle\Psi, \Psi\rangle$ equals zero for a single one. All eigenmodes would be orthogonal with respect to each other if $k_{y,2}^*$ would be replaced by $k_{y,2}$ in (12). This could be achieved as follows. Recall that if k_y is an eigenvalue with eigenmode $\binom{u'}{v'}$, then k_y^* is also an eigenvalue with eigenmode $\binom{u'^*}{-v'^*}$. Consequently, instead of (9) one could choose as inner product

$$\langle\Psi_1, \Psi_2\rangle = \int_{-\infty}^{+\infty} dx \begin{pmatrix} u_2' & v_2' \end{pmatrix} \begin{pmatrix} \tau v_t & -i\tau v_y \\ -i\tau v_y & -\tau v_t \end{pmatrix} \begin{pmatrix} u_1' \\ v_1' \end{pmatrix}. \tag{13}$$

This change does not affect the eigenmodes with real eigenvalue. However, the inner product of an eigenmode with itself is not necessarily real anymore and the physical meaning of (13) is unclear. Hence, in the remainder of this paper (9) is employed.

Note that the waveguide has been chosen to align with the y axis. Alternatively, if one would have chosen another orientation, a similar discussion about the orthogonality properties is possible. In the same way, the current in the longitudinal direction is then used to construct the inner product. Further details can be found in Appendix A.

C. Bound and radiating modes

The set of eigenmodes satisfying (3) can also be subdivided based on their behavior at infinity. This distinction is illustrated by Fig. 2. *Bound* modes decrease to zero at infinity. An example is shown in Fig. 2(b). Because of this boundary condition, only a discrete set of bound modes, represented by blue crosses in Fig. 2(a), can be found. In contrast to bound modes, *radiating* modes exhibit oscillatory or wavelike behavior at infinity, which is illustrated by Fig. 2(c). The relaxation of the boundary condition inevitably leads to a continuum of modes with eigenvalues, given by red dots in Fig. 2(a), being real or complex. The bound modes completely describe the unabated propagation of particle probability density along y within the waveguide, while the radiating modes relate to particle probability density leaking out of the waveguide's confining potential.

An important remark is in place here. As radiating modes exhibit oscillating behavior at infinity, the validity of the assumption—made in Sec. II B—that the eigenmodes vanish at infinity may be questioned. Nevertheless, a similar interpretation to that for electromagnetic eigenmodes can be invoked. One possible approach to construct the radiating modes of an electromagnetic waveguide is to surround the structure by a perfectly conducting bounding box in the transversal direction and consider the eigenmodes in the limit of an infinite-sized cross section [51]. In this paper, the radiating modes are interpreted in a similar way.

III. METHOD

To analyze the waveguide constriction based valley filter, a numerical time-stepping technique, originally developed for the conventional, time-dependent Dirac equation [50], is adapted to the case of the tilted Dirac equation (1). The time-dependent tilted Dirac equation is discretized by means of a staggered grid, where the two components of the wave function, u and v, are located at different positions in space. The spatial derivatives are approximated by fourth-order central differences to reduce dispersion errors. The resulting system of ordinary differential equations is solved by an explicit, symplectic partitioned Runge-Kutta time-stepping method [52,53], which is also fourth-order accurate [54]. Similarly as in [50], it can be demonstrated by means of Poisson maps that the resulting scheme has excellent conservation properties and that, in contrast to standard explicit Runge-Kutta time stepping, it does not introduce additional, artificial dissipation. Moreover, the explicit partitioned Runge-Kutta method does not require the storage of intermediate steps, making it an efficient method in terms of memory usage. All mathematical details are provided in Appendix B.

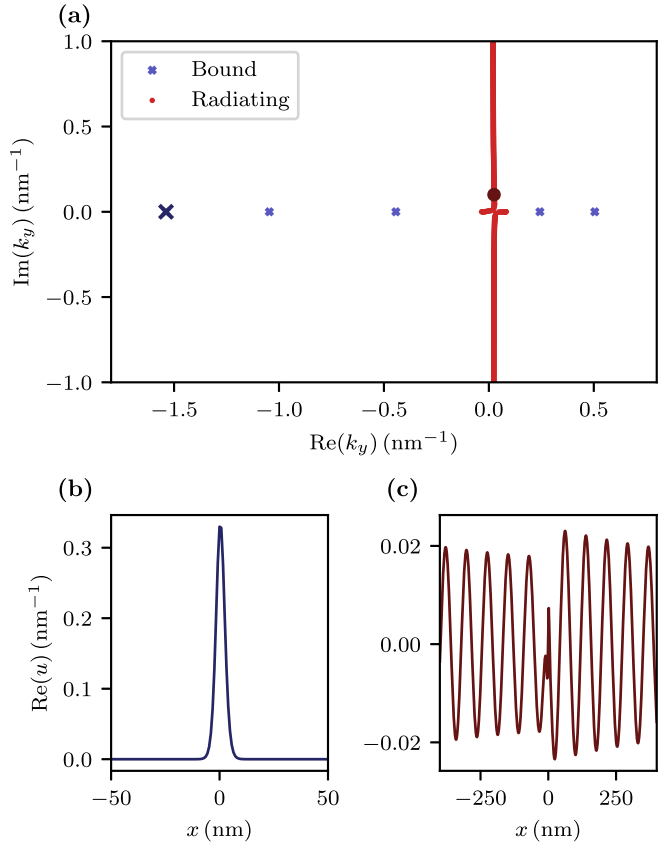

FIG. 2. (a) Eigenvalues of (3) distributed in the complex plane for valley $\boldsymbol{k}_D$. The hyperbolic secant potential (14), with $V_0 = 0.45$ eV and constant $W = 10$ nm, was chosen together with an energy E equal to -0.02 eV. (b) Plot of the real part of u as a function of the position x for the bound eigenmode associated with $k_y = -1.54\ \mathrm{nm}^{-1}$ [indicated by a large blue cross in (a)]. (c) Plot of the real part of u as a function of the position x for the radiating eigenmode associated with $k_y = (0.023 + 0.096i)\ \mathrm{nm}^{-1}$ [indicated by a large red dot in (a)].

The simulation setup of an electrostatic waveguide with nanoconstriction is depicted in Fig. 3. For the potential profile, the hyperbolic secant function is chosen

$$V(x, y) = -\frac{V_0}{\cosh[\beta(y)x]}, \tag{14}$$

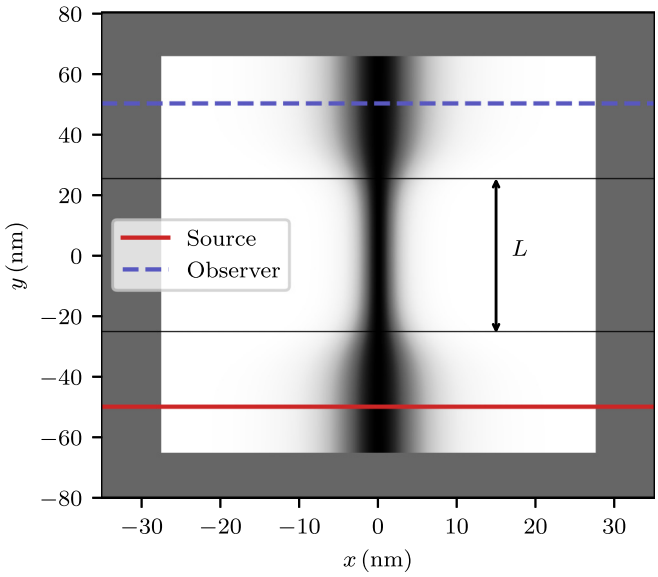

FIG. 3. Illustration of the simulation setup of an electrostatic waveguide with nanoconstriction. The middle region (black) represents a two-dimensional plot of the potential profile. The simulation domain is terminated by an absorbing layer (gray region). The constriction is of length L. The source is indicated by a red line, while the blue dashed line represents the observer.

with $\beta(y) = \frac{2\text{arccosh}(2)}{W(y)}$ and $W(y)$ is the full width at half maximum at position y, satisfying

$$W(y) = W_0 + (W_1 - W_0)\frac{1}{1 + \exp\left(\frac{|y|-L/2}{L_T}\right)}, \tag{15}$$

with W_0 and W_1 the widths outside and inside the constriction. The parameters L and L_T determine the length of the constriction and the length of the transition region, respectively. The relevance of the hyperbolic secant potential for top-gated structures has been demonstrated in [16]. It was compared to the potential of a wire suspended above a conducting plane and a good agreement was obtained.

As source a bound mode with energy E and real eigenvalue k_y is chosen, implemented by means of the total field scatter field (TFSF) approach [55]. This bound mode is injected into the electrostatic waveguide at the red line shown in Fig. 3. This incoming mode is normalized by requiring that the inner product (9) with itself is equal to 1. The $e^{-iEt/\hbar}$ time dependency of the source is further modulated by an additional Gaussian $1/(\sqrt{2\pi}\sigma_t)e^{-(t-t_0)^2/2\sigma_t^2}$, where σ_t and t_0 determine the width and the position of the Gaussian, respectively. This way, the source has a finite support in the time domain. As we intend to obtain quantitative results, such as the transmission function from one mode to another mode, an observer is added, which is indicated by the blue dashed line. Here, the outgoing wave function is transformed to the energy domain by means of the fast Fourier transform (FFT) algorithm. For every value of the energy E the resulting wave function is composed of different eigenmodes. By taking the inner product (9) of this wave function with a relevant, bound eigenmode, the associated expansion coefficient is extracted. Multiplication by its complex conjugate and additionally dividing by the spectral content of the source, a transmission function from one mode to another is obtained as a function of the energy. With this approach, a single simulation run in the time domain provides us with the transmission function for a desired range of energies.

To calculate the eigenvalues and related eigenmodes, a similar discretization procedure as for the numerical time-stepping method (see Appendix B) is applied. A staggered grid is employed together with a fourth-order central difference approximation for the spatial derivatives.

To prevent scattering at the boundaries from polluting the FFT, the simulation domain needs to be truncated by an absorbing boundary layer, which is indicated by the gray region in Fig. 3. For simplicity reasons, an absorbing potential approach is chosen, which boils down to imposing an additional *imaginary* potential near the edges [56]. In Sec. II, it was implicitly assumed that the potential $V(x)$ was real. Hence, given that the orthogonality properties are employed to calculate the transmission function, this part should be briefly revisited. It is straightforward to show that for a complex potential (12) contains an additional term

$$k_{y,1}\langle\Psi_1, \Psi_2\rangle = +k^*_{y,2}\langle\Psi_1, \Psi_2\rangle - \frac{2i}{\hbar}\int_{-\infty}^{+\infty} dx\,\text{Im}(V)(u_2'^* u_1' + v_2'^* v_1'). \tag{16}$$

If one of the two modes is a bound mode, which means that the wave function does not overlap with the imaginary potential in the absorbing layer, then the additional term disappears. Consequently, a bound mode with real eigenvalue is still orthogonal with respect to all other eigenmodes. Therefore, for the interesting case of transmission of this type of eigenmode, the above discussed procedure remains valid. Note that the eigenvalues of radiating modes that were previously real become complex in the presence of this absorbing potential because of the extra term in (16).

IV. RESULTS

A. Without constriction

We start this section by investigating the dispersion relation of the bound modes with real eigenvalues (determined by means of the numerical procedure outlined in Sec. III) for the two different valleys of 8-*Pmmn* borophene, displayed in Figs. 4(a) and 4(b). The hyperbolic secant potential (14) is employed, characterized by $V_0 = 0.45$ eV and by a full width at half maximum W independent of y and equal to 10 nm. The dispersion relation of the eigenmodes is bounded by the full black line and the dashed black line, which represent the dispersion relation of a free particle ($V = 0$) and of a particle under the influence of a constant potential $-V_0$, respectively. The absolute value of the group velocity $|dE/d\hbar k_y|$ of the forward-propagating modes in valley $\boldsymbol{k}_D$ tends to go to $v_y + v_t$, while for the backward-propagating mode this is $v_y - v_t$. For valley $-\boldsymbol{k}_D$ it is the other way around as Figs. 4(a) and 4(b) are reflections of each other with respect to the E axis.

Figures 4(c) and 4(d) focus on the lowest-order forward-propagating mode and zoom in on a particular part of the dispersion relation. The eigenvalues are plotted for different

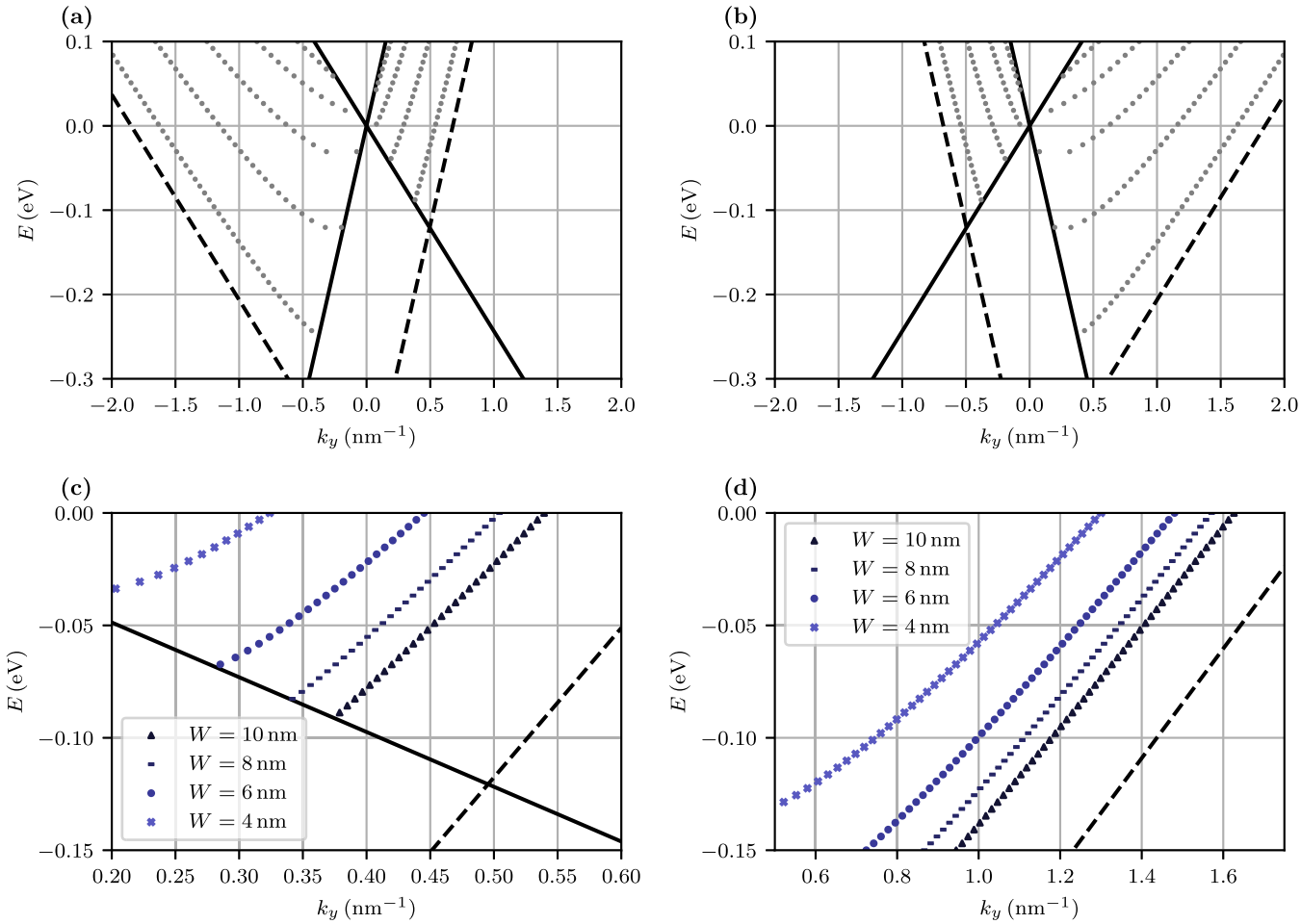

FIG. 4. (a), (b) Plots of the eigenvalues k_y of the bound modes versus energy E for the hyperbolic secant potential (14) with $W = 10$ nm and $V_0 = 0.45$ eV. (a) Gray dots represent the eigenvalues corresponding to valley $\boldsymbol{k}_D$, while in (b) the eigenvalues associated with valley $-\boldsymbol{k}_D$ are displayed. (c), (d) Plots of the eigenvalue k_y of the lowest-order, forward-propagating bound mode as a function of energy E for a set of values of the full width at half maximum W for the valleys $\boldsymbol{k}_D$ and $-\boldsymbol{k}_D$, respectively. For (a)–(d) the dispersion relation in the case of zero potential is given by the full black line. The dashed black line is the dispersion relation in the case of a constant potential $-V_0$. The eigenvalues k_y were calculated by means of the numerical procedure outlined in Sec. III.

values of the full width at half maximum W. Its effect on the dispersion relation of the eigenmodes is evident: smaller values of W shift the curve upward. From these figures it is also observed that the parameter W allows one to tune the number of bound modes propagating through the waveguide. For example, for an energy equal to -0.06 eV, the lowest-order forward-propagating bound mode for valley $-\boldsymbol{k}_D$ exists for all four indicated values of W, while for valley $\boldsymbol{k}_D$ this is not the case anymore for W equal to 4 nm.

B. With constriction

From the analysis of the previous section it becomes apparent that the structure depicted in Fig. 3 can act as a valley filter. Assume that W_0 is equal to 10 nm and W_1 is 4 nm; then for both valleys a bound mode with energy of -0.06 eV can be emitted by the source and will be propagating in the forward direction. However, only for the valley $-\boldsymbol{k}_D$, the lowest-order mode is retained in the narrow section. (Note that—in a similar fashion—the potential depth V_0 also allows one to tune the waveguide properties and thus constitutes a second approach to create valley filters.) For the aforementioned values of W_0, W_1, E, and V_0, Fig. 5 qualitatively demonstrates this effect on the propagation of a wave packet that has been constructed by modulating the lowest-order bound eigenmode by an additional Gaussian $1/(\sqrt{2\pi}\sigma_t)e^{-(t-t_0)^2/2\sigma_t^2}$, with $\sigma_t = 10$ fs and $t_0 = 50$ fs. In the case of valley $\boldsymbol{k}_D$, at 60 fs the wave packet is injected by the source into the waveguide's bottom wide section. When traversing the transition region, this incoming mode couples exclusively to radiating modes, which is shown in Fig. 5(b), as there is no forward-propagating bound mode in the narrow section. Consequently, a considerable part of the wave packet leaks out of the waveguide (and is in our simulation absorbed by the imaginary potential). At the other end of the narrow section, the radiating modes couple in the waveguide's upper, wide section to the forward-propagating bound mode [Fig. 5(c)].

In the case of the valley $-\boldsymbol{k}_D$, the incoming bound mode couples almost entirely to the forward-propagating bound mode of the narrow section thanks to the smooth transition.

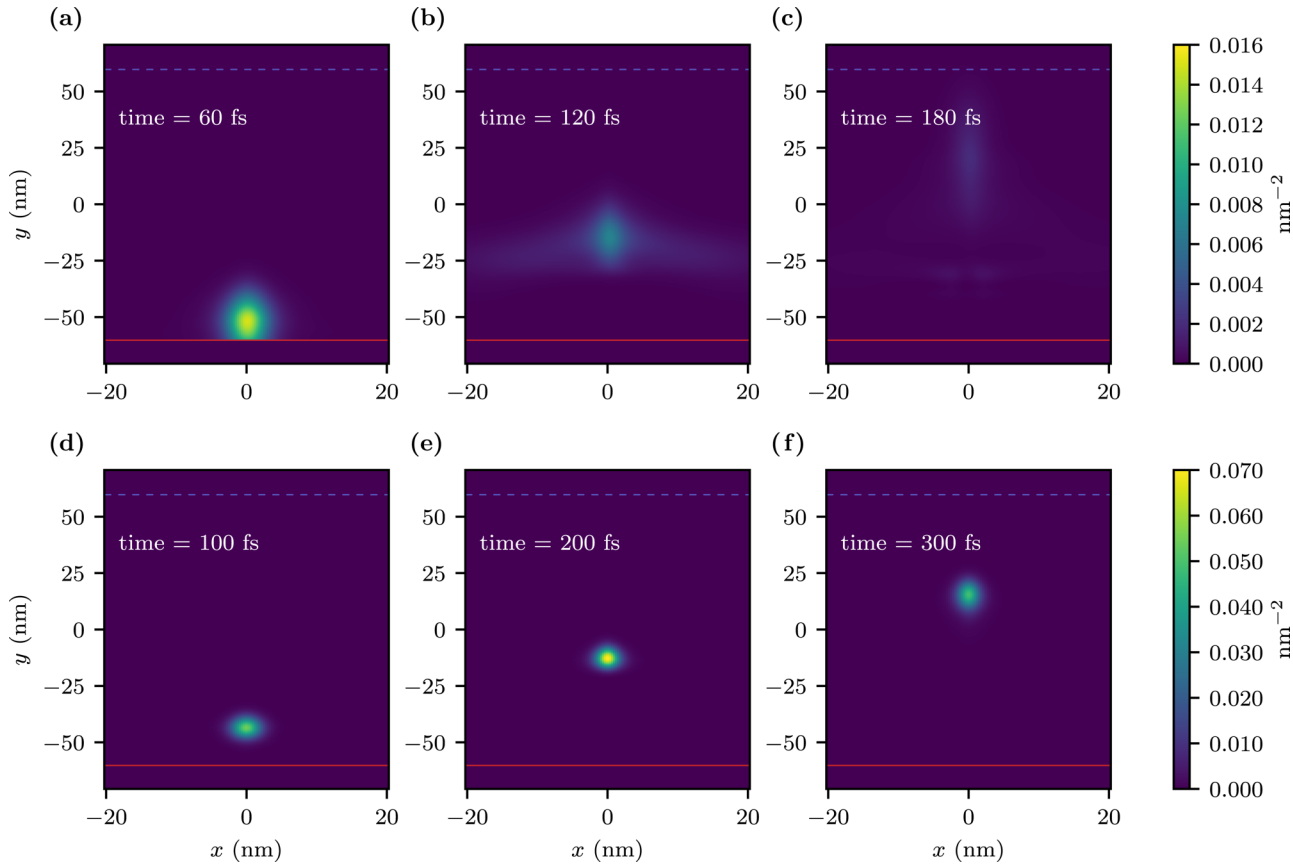

FIG. 5. (a)–(f) Snapshots of the probability density, demonstrating the valley-filtering effect of a nanoconstriction. Plots (a)–(c) are attributed to valley $\boldsymbol{k}_D$ and (d)–(f) to $-\boldsymbol{k}_D$. The potential profile corresponds to (14) with $V_0 = 0.45$ eV and with W varying with the position y according to (15). The full width at half maximum of the broad part of the potential W_0 is 10 nm, while the full width at half maximum of the narrow section W_1 equals 4 nm. The length of the narrow section L is 50 nm and the length of the transition region is characterized by $L_T = 5$ nm. The spectral content of the incoming mode is centered around $E = -0.06$ eV.

In the narrow section, the mode is better confined, leading to a brighter spot in Fig. 5(e). At 300 fs, the wave packet starts to couple into the broad waveguide section. Compared to Fig. 5(d), the wave packet is somewhat elongated along the waveguide axis due to dispersive effects. Note that the snapshots in Figs. 5(a)–5(c) and in Figs. 5(d)–5(f) are taken at different time instants because the group velocity of a forward-propagating wave packet in valley $\boldsymbol{k}_D$ approximates $v_y + v_t$, while this is $v_y - v_t$ for valley $-\boldsymbol{k}_D$.

In a next step, the valley filter is investigated from a quantitative point of view. The transmission function is determined as detailed in Sec. III and the results are shown in Fig. 6. Note that we restrict ourselves to the zero-temperature transmission function. For elevated temperatures it is expected that electron-phonon coupling plays a significant role. Hence, the effect that this electron-phonon interaction has on the valley-filtering properties of the nanoconstriction is left for future work. In Fig. 6(a), the transmission function of the two valleys is compared, while variations in the parameters W_1, L, and L_T are studied in Figs. 6(b)–6(d) for valley $\boldsymbol{k}_D$. Figure 6(a) shows that an energy window can be specified for which the transmission through the nanoconstriction equals practically 1 for valley $-\boldsymbol{k}_D$, while it is zero for $\boldsymbol{k}_D$. Hence, Fig. 6(a) demonstrates that the nanoconstriction functions as a valley filter.

In Fig. 6(b), the width of the narrow region W_1 is varied. For larger W_1, the transition from zero to perfect transmission is shifted toward more negative energies. This is completely in accordance with the results of Fig. 4(c), where it was shown that the dispersion relation of the lowest-order bound eigenmode is shifted downward for larger values of W.

The effect of the length of the narrow region L is illustrated by Fig. 6(c). For larger values of L, the transition from zero to perfect transmission is steeper. That is to say, for values of the energy E for which the narrow section does not support a forward-propagating mode, the transmission is lower for larger values of L. As in this case the injected mode couples exclusively to radiating modes, the longer the length of the constriction, the more these radiating modes diffract away from the waveguide axis, resulting in a lower transmission.

The study presented in Fig. 6(d) considers the parameter L_T, which is an indication for the length of the transition region. A larger L_T leads to a smoother transition between the modes of the broad section and those of the narrow section. Accordingly, the losses are lower for large L_T and the transmission is higher. This is clearly observed in Fig. 6(d). However, for larger values of the energy E, there are some unexpected oscillations present in the transmission function. These oscillations are more pronounced for shorter transition regions.

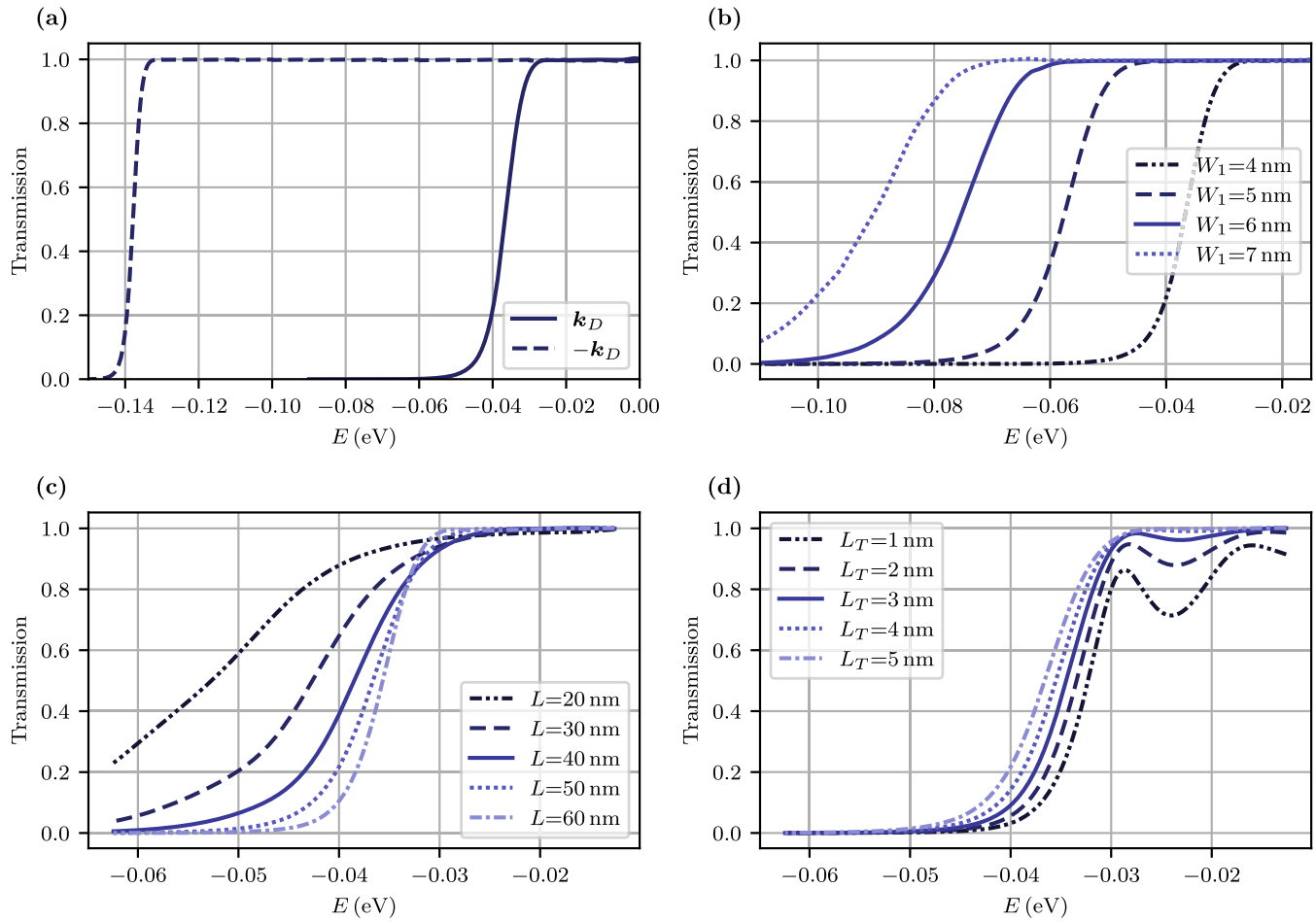

FIG. 6. Transmission through the nanoconstriction as a function of the energy E for various design parameters. The transmission for the valleys $\boldsymbol{k}_D$ and $-\boldsymbol{k}_D$ is depicted in (a) for $V_0 = 0.45$ eV, $W_0 = 10$ nm, $W_1 = 4$ nm, $L = 50$ nm, and $L_T = 5$ nm. The effect of the width of the narrow section W_1, the length of the narrow section L, and the length of the transition region are illustrated by (b), (c), and (d), respectively. In (b)–(d) the same parameters as in (a) are employed except for the one that is varied. Only valley $\boldsymbol{k}_D$ is considered in (b)–(d).

To thoroughly investigate this effect, first, a similar variation of the parameter L_T is shown in Fig. 7 but now for a

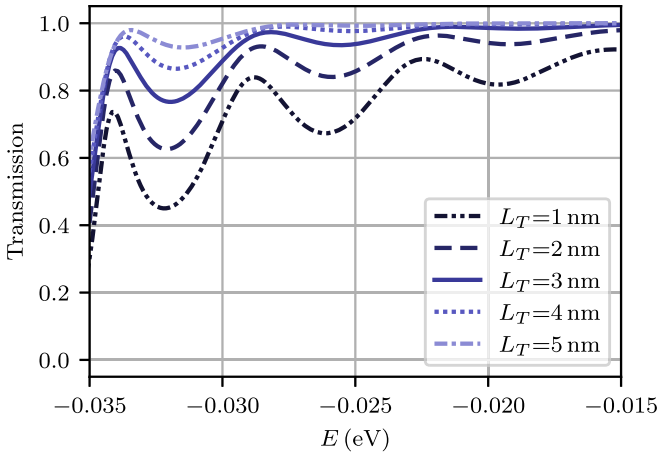

FIG. 7. Effect of the parameter L_T on the transmission through the nanoconstriction as a function of the energy E for the valley $\boldsymbol{k}_D$. The employed parameters are $V_0 = 0.45$ eV, $W_0 = 10$ nm, $W_1 = 4$ nm, and $L = 100$ nm.

constriction that is twice as long, i.e., $L = 100$ nm. The period of the oscillations has been approximately halved, indicating that the oscillations originate from interference effects. Second, Fig. 8(a) depicts a detail of the dispersion relation of the lowest-order forward-propagating bound mode for the valley $\boldsymbol{k}_D$ in the narrow part of the filter. It is observed that the dispersion relation exhibits a double mode degeneracy (one E value corresponds to two k_y values on the same dispersion curve), which explains the results of Figs. 6(d) and 7. For an energy of -0.034 eV, for example, an incoming mode can couple to two forward-propagating bound modes, indicated by a blue and red dot in the figure. As seen in Figs. 8(b) and 8(c) these modes have a similar profile as a function of the position x, however, at different length scales. Furthermore, these two forward-propagating bound modes arrive at the second transition region with a different phase. For this specific example, the phase difference approximately amounts to 2π and, thus, the modes interfere constructively at the other end of the narrow section. As a result, the transmission function clearly shows a peak at -0.034 eV in Fig. 7 for $L_T = 1$ nm. From (15) it is deduced that for smoother transitions, i.e., for larger values of L_T, the effective length of the nanoconstriction is slightly less leading to a shift of the peak to the right.

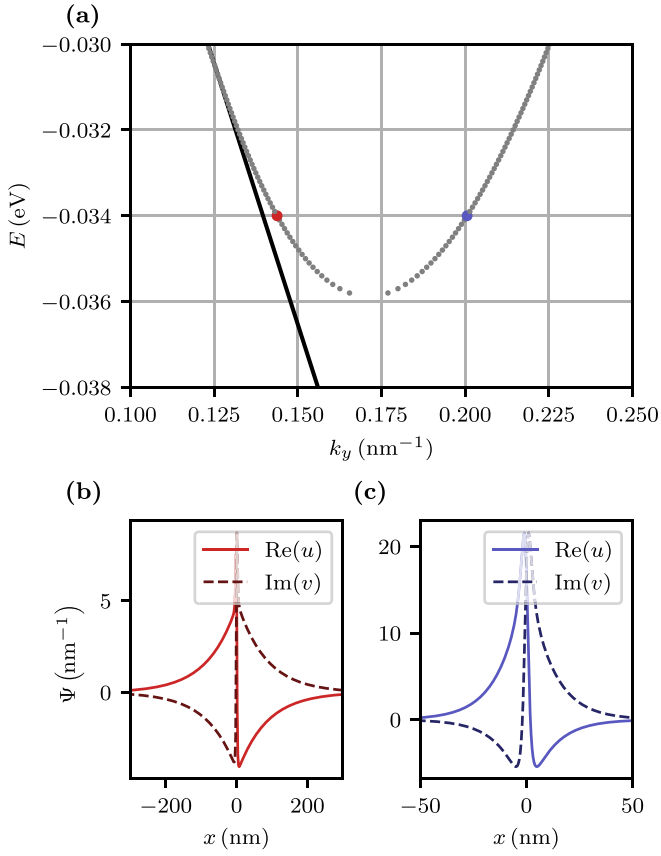

FIG. 8. (a) Detail of the dispersion relation of the lowest-order forward-propagating bound mode in a hyperbolic secant potential (14), with parameters $W = 4$ nm and $V_0 = 0.45$ eV. The eigenvalues k_y were calculated by means of the numerical procedure outlined in Sec. III. The considered valley is $\boldsymbol{k}_D$. The two eigenmodes indicated with a red and blue dot correspond to an energy E of -0.034 eV. They are plotted as a function of the position x in (b) and (c), respectively. (b) corresponds to $k_y = 0.142$ nm^{-1}, while k_y is equal to 0.200 nm^{-1} for the eigenmode presented in (c).

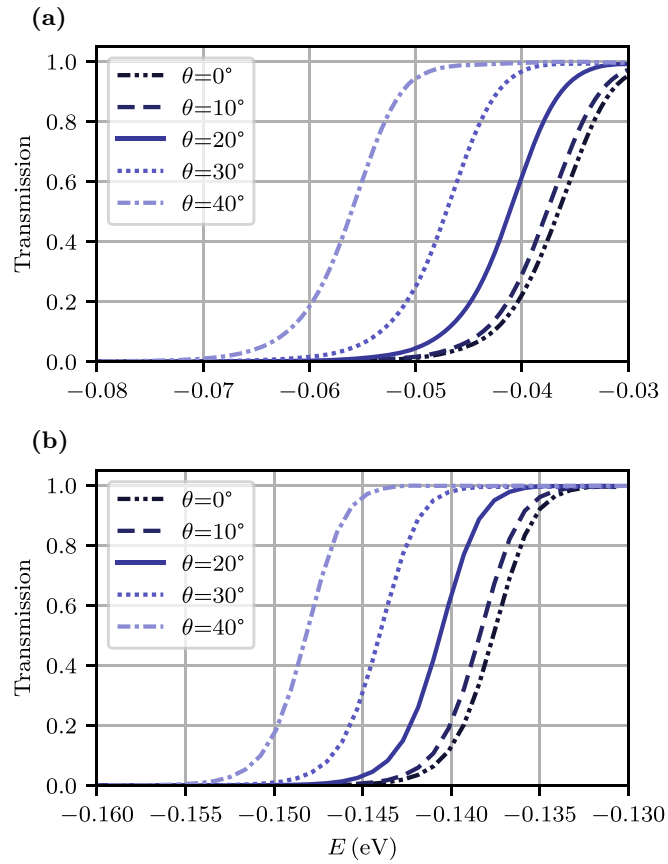

FIG. 9. Effect of the parameter θ, the angle between the axis of the waveguide and the tilting direction, on the transmission through the nanoconstriction as a function of the energy E for valley $\boldsymbol{k}_D$ (a) and valley $-\boldsymbol{k}_D$ (b). The employed parameters are $V_0 = 0.45$ eV, $W_0 = 10$ nm, $W_1 = 4$ nm, and $L = 50$ nm.

Additionally, the incoming mode couples predominantly into the mode with the largest k_y value for smoother transitions, which reduces the amplitude of the oscillations.

All previous simulations considered the situation for which the axis of the waveguide matches exactly with the tilting direction. This is the ideal scenario but it might be hard to fabricate it in a perfect way. Therefore, in a last set of simulations, we investigate the effect of θ, the angle between the axis of the waveguide and the tilting direction of the lattice. Consider the case where the waveguide is rotated in the xy plane by an angle θ, while the lattice orientation is fixed. Due to the anisotropy and the tilting, the eigenmode problem for this case has changed with respect to (3). The orthogonality relations between the eigenmodes are found in the same way as in Sec. II B, such that the numerical procedure to calculate the transmission function is still applicable. This altered eigenmode problem is further detailed in Appendix A. The results, presented in Fig. 9, indicate that for larger values of the mismatch angle θ the transmission function is shifted toward lower values of the energy. This behavior is observed for both valleys, although the shift is smaller for valley $-\boldsymbol{k}_D$. When the angle θ equals 90°, and thus when the tilting is perpendicular to the axis of the waveguide, valley filtering should be entirely absent. Hence, the transmission function of both valleys should converge toward each other for increasing mismatch angle. To investigate this behavior, the energy value for which the transmission function equals 0.5 is plotted as a function of the angle θ for both valleys in Fig. 10. It is observed that the curves indeed meet for θ equal to 90°. In addition, as both curves initially decrease for increasing mismatch angle θ, the size of the energy gap for which valley filtering is possible remains relatively large for values of θ up to 40°, making this valley filter robust against considerable misalignment of the top gate relative to the tilting direction.

V. CONCLUSION

In this paper, an alternative valley-filtering method based on electrostatic waveguides with nanoconstrictions in tilted Dirac materials, such as 8-*Pmmn* borophene, was presented. Therefore, first, the eigenmodes of an electrostatic waveguide were discussed for the tilted Dirac equation from a theoretical perspective. An inner product, based on the expression for the probability current density along the waveguide axis, was proposed, and it was shown that all bound eigenmodes are mutually orthogonal and orthogonal with respect to the

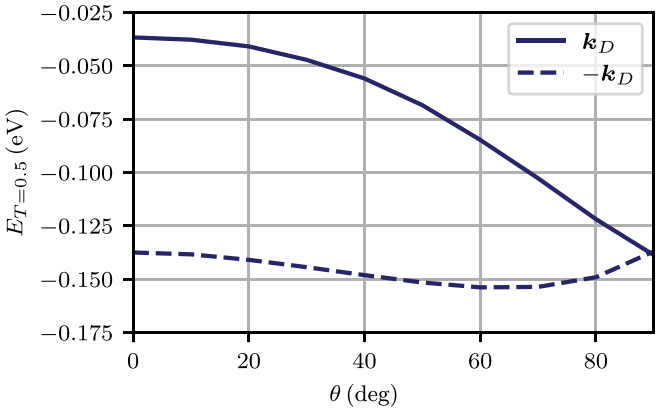

FIG. 10. Energy value $E_{T=0.5}$ for which the transmission function equals 0.5 as a function of the mismatch angle θ for both valleys $\boldsymbol{k}_D$ and $-\boldsymbol{k}_D$. The employed parameters are $V_0 = 0.45$ eV, $W_0 = 10$ nm, $W_1 = 4$ nm, and $L = 50$ nm.

radiating modes. Next, a simulation procedure based on partitioned Runge-Kutta time stepping that exploited these orthogonality relations was put forward. This simulation approach allows the calculation of the transmission function for an entire energy range with a single simulation run. Eventually, this numerical procedure was employed to study electrostatic waveguides with nanoconstrictions in tilted Dirac materials and it was demonstrated that they can indeed be used as valley filters.

The workings of the valley filter were qualitatively and quantitatively investigated. The dispersion relation for the lowest-order forward-propagating bound mode in the narrow section is shifted upward compared to the one of the wide section. Consequently, as the tilting direction is opposite in the different valleys, the geometrical parameters can be chosen such that there is no forward-propagating bound mode in the narrow section for one valley, while there is one for the other valley. As a result, for a considerably large energy window, transmission through the structure is for one valley almost nonexisting, while perfect for the other one. As it is experimentally not possible to exactly set the orientation of the top gate with respect to the lattice of the Dirac material, misalignment between the waveguide axis and tilting direction was investigated and the results showed that this energy window was robust against a mismatch angle of several tens of degrees. Three geometrical design parameters, the width of the narrow section, the length of the narrow section, and the length of the transition region, were varied and the effects were carefully examined. In addition, the simulations also revealed that the dispersion relation of the eigenmodes is not necessarily monotonic, which may give rise to oscillations in the transmission function due to interference effects.

ACKNOWLEDGMENT

The authors would like to thank Research Foundation–Flanders (FWO), Belgium, for supporting this research (Grant No. 1107321N).

APPENDIX A: EIGENMODES OF A ROTATED WAVEGUIDE

To determine the eigenmodes in a reference frame (x, y) in which the waveguide has been rotated by an angle θ with respect to the y axis, the procedure of Sec. II cannot be applied directly. Therefore, we first introduce the following coordinate transformation:

$$\begin{aligned} x' &= x\cos\theta + y\sin\theta, \\ y' &= -x\sin\theta + y\cos\theta. \end{aligned} \tag{A1}$$

The y' axis now aligns with the waveguide. Applying this coordinate transformation to the tilted Dirac equation (1) yields

$$\begin{aligned} i\hbar\frac{\partial}{\partial t}\Psi = [&\tau(v_x\sigma_x(p'_x\cos\theta - p'_y\sin\theta) \\ &+ v_y\sigma_y(p'_x\sin\theta + p'_y\cos\theta) \\ &+ v_t\sigma_0(p'_x\sin\theta + p'_y\cos\theta)) + V\sigma_0]\Psi. \end{aligned} \tag{A2}$$

Because of the y' invariance of the potential, we can substitute $u(x', y', t)$ and $v(x', y', t)$ by $u'(x')e^{i(k'_y y' - \omega t)}$ and $v'(x)e^{i(k'_y y' - \omega t)}$, respectively, resulting in the generalized eigenvalue problem

$$\begin{aligned} k'_y &\begin{pmatrix} \tau v_t\cos\theta & \tau(-v_x\sin\theta - iv_y\cos\theta) \\ \tau(-v_x\sin\theta + iv_y\cos\theta) & \tau v_t\cos\theta \end{pmatrix}\begin{pmatrix} u' \\ v' \end{pmatrix} \\ &= \begin{pmatrix} \frac{E-V(x')}{\hbar} + i\tau v_t\sin\theta\frac{d}{dx'} & \tau(iv_x\cos\theta + v_y\sin\theta)\frac{d}{dx'} \\ \tau(iv_x\cos\theta - v_y\sin\theta)\frac{d}{dx'} & \frac{E-V(x')}{\hbar} + i\tau v_t\sin\theta\frac{d}{dx'} \end{pmatrix} \\ &\quad\times\begin{pmatrix} u' \\ v' \end{pmatrix}, \end{aligned} \tag{A3}$$

with as eigenvalue k'_y and eigenmode $\binom{u'}{v'}$. To calculate the eigenmodes and associated eigenvalues, (A3) is discretized by means of a staggered grid, together with a fourth-order central difference approximation for the spatial derivatives. Afterward the eigenmode is transformed back to the original reference frame (x, y).

To determine the transmission function, the orthogonality relations of the eigenmodes are required, as explained in Sec. III. Therefore, inspired by the expression of the y' component of the probability density current

$$j'_y = \tau\Psi^\dagger(-v_x\sigma_x\sin\theta + v_y\sigma_y\cos\theta + v_t\cos\theta)\Psi, \tag{A4}$$

and similarly as in Sec. II B, we define an inner product $\langle\Psi_1, \Psi_2\rangle$ of the form

$$\int_{-\infty}^{+\infty} dx'\,\tau\Psi_2^\dagger(-v_x\sigma_x\sin\theta + v_y\sigma_y\cos\theta + v_t\cos\theta)\Psi_1. \tag{A5}$$

It is readily shown that (12) is also valid for the inner product (A5), with the eigenmodes Ψ_1 and Ψ_2 satisfying (A3). Hence,

the orthogonality properties of the eigenmodes are similar to those obtained in Sec. II B.

APPENDIX B: FOURTH-ORDER NUMERICAL METHOD FOR THE TILTED DIRAC EQUATION BASED ON PARTITIONED RUNGE-KUTTA TIME STEPPING

The spatial discretization is based on the staggered grid of [57]. The simulation domain of size $L_x \times L_y$ is subdivided into $N_x \times N_y$ unit cells. Within each unit cell (i, j) of size $\Delta x \times \Delta y$, u is defined at two positions, $(x = i\Delta x, y = j\Delta y)$ and $(x = (i + 1/2)\Delta x, y = (j + 1/2)\Delta y)$, while v is defined at $(x = (i + 1/2)\Delta x, y = j\Delta y)$ and $(x = i\Delta x, y = (j + 1/2)\Delta y)$. The corresponding values are contained in the vectors u_1, u_2, v_1, and v_2. In a next step, the spatial derivatives in the tilted Dirac equation (1) are approximated by means of a fourth-order central difference. Fourth-order averaging is applied as well so that all terms in the equation are evaluated at the same position. Splitting the components of the wave function into real and imaginary part and rearranging the resulting expression yields

$$\frac{dq}{dt} = Kp, \tag{B1}$$

$$\frac{dp}{dt} = -K^T q, \tag{B2}$$

with

$$q = \begin{pmatrix} \mathrm{Im}(u_1) \\ \mathrm{Re}(u_2) \\ \mathrm{Re}(v_1) \\ \mathrm{Im}(v_2) \end{pmatrix}, \quad p = \begin{pmatrix} \mathrm{Re}(u_1) \\ \mathrm{Im}(u_2) \\ \mathrm{Im}(v_1) \\ \mathrm{Re}(v_2) \end{pmatrix}, \tag{B3}$$

and K is equal to

$$\begin{pmatrix} \frac{-V_{u_1}}{\hbar} & -v_t A_x \otimes D_y & -v_x D_x \otimes I & v_y I \otimes D_y \\ v_t A_x^T \otimes D_y^T & \frac{V_{u_2}}{\hbar} & v_y I \otimes D_y^T & v_x D_x^T \otimes I \\ v_x D_x^T \otimes I & v_y I \otimes D_y & \frac{V_{v_1}}{\hbar} & -v_t A_x^T \otimes D_y \\ v_y I \otimes D_y^T & -v_x D_x \otimes I & v_t A_x \otimes D_y^T & \frac{-V_{v_2}}{\hbar} \end{pmatrix}. \tag{B4}$$

The Kronecker product is indicated by $\otimes$ in (B4) and V_{u_1} is a matrix with on its diagonal the values of the potential energy evaluated at the grid positions of u_1; likewise V_{u_2}, V_{v_1}, and V_{v_2} are obtained. The matrix elements of D_x satisfy the expression

$$[D_x]_{i,j} = \frac{1}{24\Delta x}(\delta_{i,j-2} - 27\delta_{i,j-1} + 27\delta_{i,j} - \delta_{i,j+1}), \tag{B5}$$

with i and j varying from 1 to N_x. The elements of A_x are given by

$$[A_x]_{i,j} = \tfrac{1}{16}(-\delta_{i,j-2} + 9\delta_{i,j-1} + 9\delta_{i,j} - \delta_{i,j+1}). \tag{B6}$$

Because of the specific form of the set of equations (B1) and (B2) an explicit, symplectic partitioned Runge-Kutta time-stepping method can be used [52,53]. Stepping in time from $t = n\Delta t$ to $t = (n + 1)\Delta t$ corresponds to

$$\begin{aligned} Q^{n,0} &= q^n, & P^{n,1} &= p^n, \\ Q^{n,1} &= Q^{n,0} + \Delta t\, B_1\, K P^{n,1}, & P^{n,2} &= P^{n,1} - \Delta t\, b_1\, K^T Q^{n,1}, \\ Q^{n,2} &= Q^{n,1} + \Delta t\, B_2\, K P^{n,2}, & P^{n,3} &= P^{n,2} - \Delta t\, b_2\, K^T Q^{n,2}, \\ &\vdots & &\vdots \\ Q^{n,s} &= Q^{n,s-1} + \Delta t\, B_s\, K P^{n,s}, & P^{n,s+1} &= P^{n,s} - \Delta t\, b_s\, K^T Q^{n,s}, \\ q^{n+1} &= Q^{n,s}, & p^{n+1} &= P^{n,s+1}, \end{aligned} \tag{B7}$$

where the intermediate values are denoted by capital letters. The constants b_i and B_i, where i ranges from 1 to s, the number of substeps, characterize the partitioned Runge-Kutta method. In this work, a fourth-order method is employed from [50,54].

Note that (B1) and (B2) can be rewritten as a Poisson system, similarly as for the normal Dirac equation [50]. Hence, it is readily shown, following the same steps as in [50], that this numerical method based on partitioned Runge-Kutta time stepping conserves the probability and energy up to the fourth order of the time step and that it, in contrast to explicit Runge-Kutta time stepping, does not lead to additional, spurious dissipation.

[1] T. O. Wehling, A. M. Black-Schaffer, and A. V. Balatsky, Dirac materials, Adv. Phys. **63**, 1 (2014).

[2] P. E. Allain and J. N. Fuchs, Klein tunneling in graphene: Optics with massless electrons, Eur. Phys. J. B **83**, 301 (2011).

[3] V. Cheianov, V. Fal'ko, and B. Altshuler, The focusing of electron flow and a Veselago lens in graphene *p-n* junctions, Science **315**, 1252 (2007).

[4] M. S. Jang, H. Kim, Y. W. Son, H. A. Atwater, and W. A. Goddard, Graphene field effect transistor without an energy gap, Proc. Natl. Acad. Sci. USA **110**, 8786 (2013).

[5] Q. Wilmart, S. Berrada, D. Torrin, V. H. Nguyen, G. Fève, J. M. Berroir, P. Dollfus, and B. Plaçais, A Klein-tunneling transistor with ballistic graphene, 2D Mater. **1**, 011006 (2014).

[6] Y. Tan, M. M. Elahi, H. Y. Tsao, K. M. Habib, N. S. Barker, and A. W. Ghosh, Graphene Klein tunnel transistors for high speed analog RF applications, Sci. Rep. **7**, 9714 (2017).

[7] M. M. Elahi, K. M. M. Habib, K. Wang, G. H. Lee, P. Kim, and A. W. Ghosh, Impact of geometry and non-idealities on electron "optics" based graphene *p-n* junction devices, Appl. Phys. Lett. **114**, 013507 (2019).

[8] S. Morikawa, Q. Wilmart, S. Masubuchi, K. Watanabe, T. Taniguchi, B. Plaçais, and T. Machida, Dirac fermion reflector by ballistic graphene sawtooth-shaped npn junctions, Semicond. Sci. Technol. **32**, 045010 (2017).

[9] A. F. Young and P. Kim, Quantum interference and Klein tunnelling in graphene heterojunctions, Nat. Phys. **5**, 222 (2009).

[10] S. Chen, Z. Han, M. M. Elahi, K. M. M. Habib, L. Wang, B. Wen, Y. Gao, T. Taniguchi, K. Watanabe, J. Hone, A. W. Ghosh, and C. R. Dean, Electron optics with *p-n* junctions in ballistic graphene, Science **353**, 1522 (2016).

[11] C. W. J. Beenakker, R. A. Sepkhanov, A. R. Akhmerov, and J. Tworzydło, Quantum Goos-Hänchen effect in graphene, Phys. Rev. Lett. **102**, 146804 (2009).

[12] X. Chen, X. J. Lu, Y. Ban, and C. F. Li, Electronic analogy of the Goos-Hänchen effect: A review, J. Opt. **15**, 033001 (2013).

[13] Y. Ren, P. Wan, L. Zhou, R. Zhao, Q. Wang, D. Huang, H. Guo, and J. Du, Zero-index metamaterials for Dirac fermion in graphene, Phys. Rev. B **103**, 085431 (2021).

[14] E. Paredes-Rocha, Y. Betancur-Ocampo, N. Szpak, and T. Stegmann, Gradient-index electron optics in graphene *p-n* junctions, Phys. Rev. B **103**, 045404 (2021).

[15] F. M. Zhang, Y. He, and X. Chen, Guided modes in graphene waveguides, Appl. Phys. Lett. **94**, 212105 (2009).

[16] R. R. Hartmann, N. J. Robinson, and M. E. Portnoi, Smooth electron waveguides in graphene, Phys. Rev. B **81**, 245431 (2010).

[17] Y. He, Y. Xu, Y. Yang, and W. Huang, Guided modes in asymmetric graphene waveguides, Appl. Phys. A: Mater. Sci. Process. **115**, 895 (2014).

[18] P. Rickhaus, M. H. Liu, P. Makk, R. Maurand, S. Hess, S. Zihlmann, M. Weiss, K. Richter, and C. Schönenberger, Guiding of electrons in a few-mode ballistic graphene channel, Nano Lett. **15**, 5819 (2015).

[19] R. R. Hartmann and M. E. Portnoi, Two-dimensional Dirac particles in a Pöschl-Teller waveguide, Sci. Rep. **7**, 11599 (2017).

[20] A. Cheng, T. Taniguchi, K. Watanabe, P. Kim, and J. D. Pillet, Guiding Dirac fermions in graphene with a carbon nanotube, Phys. Rev. Lett. **123**, 216804 (2019).

[21] R. R. Hartmann and M. E. Portnoi, Bipolar electron waveguides in graphene, Phys. Rev. B **102**, 155421 (2020).

[22] E. Vanderstraeten and D. Vande Ginste, Analysis of electronic waveguide bends in graphene subject to Dirac point fluctuations, in *2022 IEEE International Conference on Emerging Electronics (ICEE)* (IEEE, Bangalore, India, 2022), pp. 1–4.

[23] Y. He, M. Ding, Y. Yang, and H. Zhang, Guided modes in a graphene barrier waveguide, Superlattice. Microst. **85**, 761 (2015).

[24] Z. Jalali-Mola and S. A. Jafari, Tilt-induced kink in the plasmon dispersion of two-dimensional Dirac electrons, Phys. Rev. B **98**, 195415 (2018).

[25] S. Katayama, A. Kobayashi, and Y. Suzumura, Pressure-induced zero-gap semiconducting state in organic conductor α-(BEDT-TTF)$_2$I$_3$ salt, J. Phys. Soc. Jpn. **75**, 054705 (2006).

[26] M. O. Goerbig, J. N. Fuchs, G. Montambaux, and F. Piéchon, Tilted anisotropic Dirac cones in quinoid-type graphene and α-(BEDT-TTF)$_2$I$_3$, Phys. Rev. B **78**, 045415 (2008).

[27] K. Kajita, Y. Nishio, N. Tajima, Y. Suzumura, and A. Kobayashi, Molecular Dirac fermion systems theoretical and experimental approaches, J. Phys. Soc. Jpn. **83**, 072002 (2014).

[28] H. Y. Lu, A. S. Cuamba, S. Y. Lin, L. Hao, R. Wang, H. Li, Y. Y. Zhao, and C. S. Ting, Tilted anisotropic Dirac cones in partially hydrogenated graphene, Phys. Rev. B **94**, 195423 (2016).

[29] X. F. Zhou, X. Dong, A. R. Oganov, Q. Zhu, Y. Tian, and H. T. Wang, Semimetallic two-dimensional boron allotrope with massless Dirac fermions, Phys. Rev. Lett. **112**, 085502 (2014).

[30] A. Lopez-Bezanilla and P. B. Littlewood, Electronic properties of 8-*Pmmn* borophene, Phys. Rev. B **93**, 241405(R) (2016).

[31] A. D. Zabolotskiy and Y. E. Lozovik, Strain-induced pseudomagnetic field in the Dirac semimetal borophene, Phys. Rev. B **94**, 165403 (2016).

[32] Z. Q. Wang, T. Y. Lu, H. Q. Wang, Y. P. Feng, and J. C. Zheng, Band gap opening in 8-*Pmmn* borophene by hydrogenation, ACS Appl. Electron. Mater. **1**, 667 (2019).

[33] D. Wang, A. Hu, J. P. Lv, and G. Jin, Electric field modulated valley- and spin-dependent electron retroreflection and Klein tunneling in a tilted *n-p-n* junction of monolayer 1T'-MoS_2, Phys. Rev. B **107**, 035301 (2023).

[34] A. J. Mannix, X.-F. Zhou, B. Kiraly, J. D. Wood, D. Alducin, B. D. Myers, X. Liu, B. L. Fisher, U. Santiago, J. R. Guest, M. J. Yacaman, A. Ponce, A. R. Oganov, M. C. Hersam, and N. P. Guisinger, Synthesis of borophenes: Anisotropic, two-dimensional boron polymorphs, Science **350**, 1513 (2015).

[35] P. Ranjan, T. K. Sahu, R. Bhushan, S. S. Yamijala, D. J. Late, P. Kumar, and A. Vinu, Freestanding borophene and its hybrids, Adv. Mater. **31**, 1900353 (2019).

[36] S. Y. Xie, Y. Wang, and X. B. Li, Flat boron: A new cousin of graphene, Adv. Mater. **31**, 1900392 (2019).

[37] S. Chahal, P. Ranjan, M. Motlag, S. S. Yamijala, D. J. Late, E. H. S. Sadki, G. J. Cheng, and P. Kumar, Borophene via micromechanical exfoliation, Adv. Mater. **33**, 2102039 (2021).

[38] X. Liu, Q. Li, Q. Ruan, M. S. Rahn, B. I. Yakobson, and M. C. Hersam, Borophene synthesis beyond the single-atomic-layer limit, Nat. Mater. **21**, 35 (2022).

[39] S. H. Zhang and W. Yang, Oblique Klein tunneling in 8-*Pmmn* borophene *p-n* junctions, Phys. Rev. B **97**, 235440 (2018).

[40] X. Zhou, Valley-dependent electron retroreflection and anomalous Klein tunneling in an 8-*Pmmn* borophene-based *n-p-n* junction, Phys. Rev. B **100**, 195139 (2019).

[41] S. H. Zhang and W. Yang, Anomalous caustics and Veselago focusing in 8-*Pmmn* borophene *p-n* junctions with arbitrary junction directions, New J. Phys. **21**, 103052 (2019).

[42] Z. Kong, J. Li, Y. Zhang, S. H. Zhang, and J. J. Zhu, Oblique and asymmetric Klein tunneling across smooth *np* junctions or *npn* junctions in 8-*Pmmn* borophene, Nanomaterials **11**, 1462 (2021).

[43] G. N. Yu, G. Y. Yi, W. B. Cui, L. L. Zhang, X. S. Li, and W. J. Gong, Quantum transmission through the *n-p-n* heterojunction of massive 8-*Pmmn* borophene, J. Phys.: Condens. Matter **34**, 085401 (2022).

[44] C. Zhang, J. Yang, S. H. Zhang, and W. Yang, Goos-Hänchen shift of electron waves reflected by 8-*Pmmn* borophene *np* junctions, J. Appl. Phys. **132**, 184302 (2022).

[45] X. Zhou, J. Zheng, and F. Zhai, Anisotropic and valley-resolved beam-splitter based on a tilted Dirac system, Commun. Theor. Phys. **74**, 075701 (2022).

[46] J. Zheng, J. Lu, F. Zhai, and F. Zhai, Anisotropic and gate-tunable valley filtering based on 8-*Pmmn* borophene, Nanotechnology **32**, 025205 (2021).

[47] Y. Xu, Y. Fang, and G. Jin, Valley-polarized and super-collimated electronic transport in an 8-*Pmmn* borophene superlattice, New J. Phys. **25**, 013020 (2023).

[48] K. K. Bai, J. J. Zhou, Y. C. Wei, J. B. Qiao, Y. W. Liu, H. W. Liu, H. Jiang, and L. He, Generating atomically sharp *p-n*

junctions in graphene and testing quantum electron optics on the nanoscale, Phys. Rev. B **97**, 045413 (2018).

[49] R. A. Ng, A. Wild, M. E. Portnoi, and R. R. Hartmann, Quasi-exact solutions for guided modes in two-dimensional materials with tilted Dirac cones, Sci. Rep. **12**, 7688 (2022).

[50] E. Vanderstraeten and D. V. Ginste, A conservative fourth-order real space method for the (2+1)D Dirac equation, J. Comput. Appl. Math. **428**, 115149 (2023).

[51] A. W. Snyder and J. D. Love, *Optical Waveguide Theory*, 1st ed. (Chapman and Hall, London, UK, 1983).

[52] J. M. Sanz-Serna and M. P. Calvo, *Numerical Hamiltonian Problems*, 1st ed. (Chapman and Hall, London, UK, 1994).

[53] B. Leimkuhler and S. Reich, *Simulating Hamiltonian Dynamics*, Cambridge Monographs on Applied and Computational Mathematics (Cambridge University Press, Cambridge, UK, 2005).

[54] R. I. McLachlan, On the numerical integration of ordinary differential equations by symmetric composition methods, SIAM J. Sci. Comput. **16**, 151 (1995).

[55] A. Taflove and S. C. Hagness, *Computational Electrodynamics: The Finite-Difference Time-Domain Method*, 3rd ed. (Artech House, London, UK, 2005).

[56] O. Pinaud, Absorbing layers for the Dirac equation, J. Comput. Phys. **289**, 169 (2015).

[57] R. Hammer, W. Pötz, and A. Arnold, Single-cone real-space finite difference scheme for the time-dependent Dirac equation, J. Comput. Phys. **265**, 50 (2014).